# Targeted search for the kinematic dipole of the gravitational-wave background

Adrian Ka-Wai Chung,[1,*] Alexander C. Jenkins,[2,†] Joseph D. Romano,[3,‡] and Mairi Sakellariadou[1,§]

[1]*Theoretical Particle Physics and Cosmology Group, Physics Department, King's College London, University of London, Strand, London WC2R 2LS, United Kingdom*

[2]*Department of Physics and Astronomy, University College London, London WC1E 6BT, United Kingdom*

[3]*Department of Physics and Astronomy, Texas Tech University, Box 41051, Lubbock, Texas 79409-1051, USA*

(Received 3 August 2022; accepted 28 September 2022; published 21 October 2022)

There is growing interest in using current and future gravitational-wave interferometers to search for anisotropies in the gravitational-wave background. One guaranteed anisotropic signal is the kinematic dipole induced by our peculiar motion with respect to the cosmic rest frame, as measured in other full-sky observables such as the cosmic microwave background. Our prior knowledge of the amplitude and direction of this dipole is not explicitly accounted for in existing searches by LIGO/Virgo/KAGRA but could provide crucial information to help disentangle the sources which contribute to the gravitational-wave background. Here, we develop a targeted search pipeline which uses this prior knowledge to enable unbiased and minimum-variance inference of the dipole magnitude. Our search generalizes existing methods to allow for a time-dependent signal model, which captures the annual modulation of the dipole due to the Earth's orbit. We validate our pipeline on mock data, demonstrating that neglecting this time dependence can bias the inferred dipole by as much as $\mathcal{O}(10\%)$. We then run our analysis on the full LIGO/Virgo O1 + O2 + O3 dataset, obtaining upper limits on the dipole amplitude that are consistent with existing anisotropic search results.

DOI: 10.1103/PhysRevD.106.082005

## I. INTRODUCTION

The direct detection of gravitational waves (GWs) from compact binary coalescences by the LIGO/Virgo/KAGRA Collaboration (LVK) has initiated the era of GW astronomy [1–4]. As well as transient, individually resolvable signals such as these, one also expects a gravitational-wave background (GWB) due to the superposition of GWs produced by many weak, independent, and unresolved sources of cosmological or astrophysical origin [5–9]. Once detected, this background will provide interesting astrophysical information about the formation of black holes and neutron stars throughout cosmic time [10,11] and will potentially shed light on early universe cosmology and particle physics beyond the Standard Model [12–17].

In order to extract as much of this information as possible from the GWB, we must study not only its mean intensity but also the fluctuations in this intensity across the sky—the *anisotropies* in the GWB. There has been much recent interest in studying the "intrinsic" anisotropies due to statistical clustering of GW sources, particularly for the astrophysical GWB from coalescing compact binaries [18–30]. However, as first pointed out in [31,32], the relatively small number of compact binaries in the observable Universe means that measurements of these anisotropies suffer from very high levels of shot noise, limiting the astrophysical and cosmological information that can be extracted from them.

Aside from the intrinsic anisotropies, there are also *extrinsic* or *kinematic* anisotropies due to the peculiar motion of our GW detectors with respect to the rest frame of the GWB [20,23,33–35]. Most notable of these is the Doppler enhancement of the GW intensity we observe from sources we are moving toward and the corresponding reduction in intensity from sources we are receding from. This generates a *kinematic dipole* in the GWB. This effect is well known and has been measured with high precision in other cosmological observables, particularly the cosmic microwave background (CMB) [36]. As we discuss below, a joint measurement of this dipole and of the monopole could help us unravel the physics of the sources that contribute to the GWB, as well as potentially shedding light on the existing tension between the CMB dipole and the dipole observed in source counts of quasars and radio galaxies [37–39] (see however [40]).

*ka-wai.chung@ligo.org
†alex.jenkins@ucl.ac.uk
‡joseph.d.romano@ttu.edu
§mairi.sakellariadou@kcl.ac.uk

 

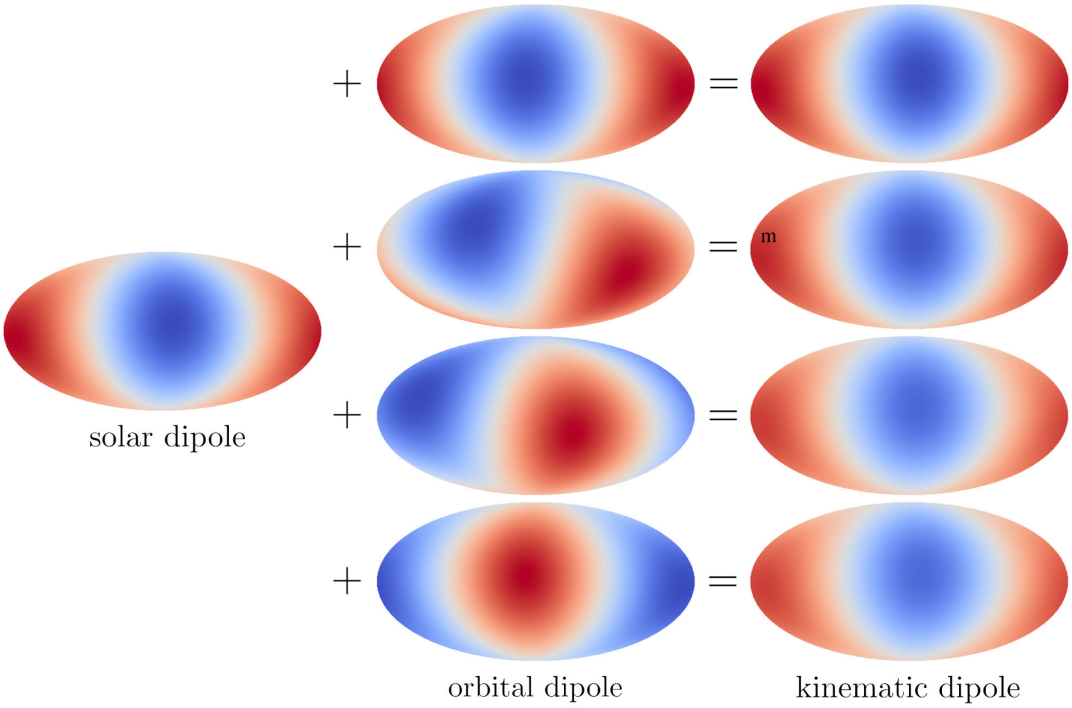


FIG. 1. The kinematic dipole is a superposition between a (time-independent) *solar dipole* and a (time-dependent) *orbital dipole*. Here, we show the orbital dipole at 0, 2, 4, and 6 months from the time at which the Earth is at perihelion (reading from top to bottom), with the amplitude of the total dipole becoming progressively smaller over this time. The resulting $\mathcal{O}(10\%)$ variation is difficult to distinguish by eye here but has a significant impact on the search, as demonstrated in Fig. 2.

We present here a targeted search method to measure the GWB kinematic dipole. In Sec. II, we construct a signal model of the dipole by considering both the (constant) motion of the solar system barycenter with respect to the cosmic rest frame and the (time-dependent) orbital motion of the Earth around this barycenter, as illustrated in Fig. 1. In Sec. III, we develop a maximum-likelihood estimator for the mean dipole amplitude, extending the existing data-analysis search formalism [7,41] to allow for a time-dependent signal. In Sec. IV, we validate our formalism on mock data, before running our analysis on the first three observing runs (O1, O2, O3) of the Advanced LIGO and Advanced Virgo interferometers. We summarize our conclusions in Sec. V.

We work in relativistic units, $c = 1$, throughout. Following [41–46], we assume the *Planck* 2015 value of the Hubble constant, $H_0 = 67.9\ \mathrm{km\,s^{-1}\,Mpc^{-1}}$ [47].

## II. SIGNAL MODEL

### A. The monopole

We characterize the isotropic (monopole) component of the GWB in terms of its energy density spectrum [measured in units of the cosmological critical energy density $\rho_c \equiv 3H_0^2/(8\pi G)$],

$$\Omega(f) \equiv \frac{1}{\rho_c}\frac{\mathrm{d}\rho_{\mathrm{gw}}}{\mathrm{d}(\ln f)}. \tag{1}$$

We calculate this spectrum in terms of quantities describing the GW sources by writing [48]

$$\Omega(f) = \frac{1}{\rho_c}\int_0^\infty \frac{\mathrm{d}z}{(1+z)^2}\int d\boldsymbol{\vartheta}\,\frac{\mathcal{R}(z,\boldsymbol{\vartheta})}{H(z)}\frac{\mathrm{d}E(\boldsymbol{\vartheta})}{\mathrm{d}(\ln f_s)}, \tag{2}$$

where $H(z)$ is the Hubble rate, $\boldsymbol{\vartheta}$ a set of parameters characterizing the sources, $\mathcal{R}$ the comoving source rate density, and $\mathrm{d}E/\mathrm{d}(\ln f_s)$ the spectrum of the radiated GW energy in terms of the source-frame frequency $f_s = (1+z)f$.

For simplicity, we assume that this spectrum is well approximated by a power law throughout our sensitive frequency band,[1]

$$\Omega(f) = \Omega_\alpha (f/f_{\mathrm{ref}})^\alpha, \tag{3}$$

with $\Omega_\alpha$ giving the GWB amplitude at some reference frequency $f_{\mathrm{ref}}$ (following [41–46], we use $f_{\mathrm{ref}} = 25$ Hz throughout). LVK stochastic analyses typically focus on three $\alpha$ values of particular interest:

(i) $\alpha = 0$, which corresponds to a scale-invariant background (i.e., $\Omega =$ constant). This is approximately what one expects for a GWB signal from

[1]Note that this power-law assumption is *not* essential to our search and can easily be replaced with a generic spectral ansatz.

Nambu-Goto cosmic string loops at high frequencies [13] and is also characteristic of (single-field, slow-roll) inflationary models [5,6].

(ii) $\alpha = 2/3$, which corresponds to a (slightly) blue-tilted spectrum. This is a robust prediction for the astrophysical GWB from inspiraling (populations I or II) compact binaries [10].

(iii) $\alpha = 3$, which corresponds to a white noise strain power spectral density $S_{\rm gw}(f) \propto \Omega(f)/f^3 = \text{const.}$ This has been studied as an approximation to the astrophysical GWB from core-collapse supernovae [49].

In the following sections, we present results for each of these three spectral indices.

### B. The kinematic dipole

The Earth's peculiar motion with respect to the GWB rest frame induces a small, time-dependent anisotropic contribution to the observed GWB, linearly superimposed on the time-independent isotropic component described above. We write this kinematic dipole as the sum of two contributions: one due to the motion of the solar system barycenter (which does not vary appreciably over observational timescales) and the other due to the motion of the Earth around this barycenter (which undergoes annual modulation). As in [36], we call these the "solar dipole" and "orbital dipole", respectively. Hence, the dipole density parameter can be written as[2]

$$\Omega^{(\rm d)}(f,t,\hat{\boldsymbol{r}}) = \mathcal{D}(f)\left[\hat{\boldsymbol{r}}\cdot\hat{\boldsymbol{r}}_{\rm sol} + \frac{\hat{\boldsymbol{r}}\cdot\boldsymbol{v}_{\rm orb}(t)}{v_{\rm sol}}\right], \tag{4}$$

where $\hat{\boldsymbol{r}}_{\rm sol}$ is a unit vector pointing in the direction of the solar dipole, $v_{\rm sol}$ the peculiar velocity of the solar system barycenter in that direction, and $\boldsymbol{v}_{\rm orb}$ the Earth's orbital velocity vector around the barycenter as a function of time.

One can show that, for a power-law monopole signal of the kind we are considering here, the amplitude of the dipole follows the same power law in frequency [20,23],

$$\mathcal{D}(f) = \mathcal{D}_\alpha (f/f_{\rm ref})^\alpha. \tag{5}$$

In the case of CMB temperature anisotropies, the magnitude of the dipole is trivially related to the monopole by a factor of $v_{\rm sol}$, due to the behavior of the thermal black-body spectrum under Lorentz boosts. For the GWB, this is generally not the case. In fact, one can show that [34]

$$\mathcal{D}(f) = \frac{v_{\rm sol}}{4\pi}\left(4 - \frac{\partial}{\partial(\ln f_{\rm s})}\right)\Omega(f) + \mathcal{O}v_{\rm sol}^3, \tag{6}$$

where the derivative should be understood as being taken inside the double integral which defines the monopole $\Omega(f)$ in Eq. (2).[3] (We have included only the linear-order term here, since $v_{\rm sol} \sim 10^{-3}$ in relativistic units. See [33] for a recent discussion of higher-order kinematic effects in the GWB.)

As a simple, specific example, consider the GWB generated by inspiraling compact binaries. Here, all of the binaries emit GWs with the same $\alpha = 2/3$ spectrum, so we find

$$\mathcal{D}_{2/3} = (5/6\pi) v_{\rm sol} \Omega_{2/3}. \tag{7}$$

This relationship between the dipole and monopole amplitudes is a robust and nontrivial prediction for the compact binary GWB. A measurement of the dipole amplitude is therefore a valuable consistency check against an observed monopole signal: for example, if the inferred value of $\mathcal{D}_{2/3}$ were to disagree with Eq. (7), this would point to either a deviation from the $\sim f^{2/3}$ power law expected from inspiraling compact binaries[4] or a disagreement between the true solar dipole velocity $v_{\rm sol}$ and the value inferred by CMB observations, either of which would be a significant and interesting result.

More generally, the fact that each GW source has a different multiplicative factor relating the monopole and dipole amplitudes means that, in principle, a joint measurement of both could reveal the physics of the sources that contribute to the GWB. This implies that a targeted search for the dipole is extremely useful: despite being an "extrinsic" effect due to the observer, it contains valuable astrophysical and cosmological information.

### C. The solar dipole

We now calculate the dipole induced by the motion of the Sun relative to the cosmic rest frame. In doing so, it is convenient to work in spherical harmonics,

$$\Omega^{(\rm d)}_{\ell m} = (f/f_{\rm ref})^{-\alpha} \int_{S^2} {\rm d}^2\hat{\boldsymbol{r}} Y^*_{\ell m}(\hat{\boldsymbol{r}}) \Omega^{(\rm d)}(f,t,\hat{\boldsymbol{r}}), \tag{8}$$

where we have factored out the frequency dependence.

[2]Note that $\Omega^{(\rm d)}$ is a distribution on the sky and therefore has units of GWB energy density *per unit solid angle*. This amounts to a factor $4\pi$ difference in normalization compared to the monopole.

[3]The fact that the derivative is evaluated in this way means that this term is not necessarily proportional to $\alpha$. For example, in the case of cosmic strings, the energy radiated by each string loop is *not* scale invariant, so this derivative term is nonzero [20]. The monopole is only (approximately) scale invariant due to the interplay of the energy spectrum of each loop, the scaling distribution of loop sizes, and the expansion of the Universe.

[4]Such deviations could be caused by, e.g., a larger-than-expected contribution from massive binaries which merge within the LIGO/Virgo frequency band [50] or perhaps additional energy loss channels during the inspiral, such as friction effects from the binary's astrophysical environment [51] or coupling to fundamental fields beyond the Standard Model [52].

The right ascension and declination of the solar dipole in equatorial coordinates [chosen to match the spherical harmonic decomposition in Eq. (23)], as inferred by *Planck* [36], are

$$(\alpha_{\rm sol},\delta_{\rm sol}) = (167.942 \pm 0.007, -6.944 \pm 0.007)\ \text{deg}. \quad (9)$$

Neglecting the orbital dipole for now, this allows us to derive the spherical harmonics associated with the solar dipole,

$$\begin{aligned}\Omega_{10}^{(\rm sol)} &= \sqrt{\frac{4\pi}{3}}\cos(\pi/2-\delta_{\rm sol})\mathcal{D}_\alpha \\ &= -0.24744\mathcal{D}_\alpha, \\ \Omega_{11}^{(\rm sol)} &= -\sqrt{\frac{2\pi}{3}}\sin(\pi/2-\delta_{\rm sol})e^{-i\alpha_{\rm sol}}\mathcal{D}_\alpha \\ &= (1.40489 + 0.30011i)\mathcal{D}_\alpha, \end{aligned} \quad (10)$$

with $\Omega_{1,-1}^{(\rm sol)} = -\Omega_{11}^{(\rm sol)*}$ and all other harmonics equal to zero.

### D. The orbital dipole

Let us now include the orbital dipole induced by the motion of the Earth relative to the solar system barycenter. We write the Earth's orbital velocity as

$$\boldsymbol{v}_{\rm orb} = \frac{\omega a}{\sqrt{1-e^2}}[-\sin\psi\,\hat{\boldsymbol{x}} + (\cos\psi + e)\hat{\boldsymbol{y}}], \quad (11)$$

where $\omega \equiv 2\pi/T_{\rm orb}$ is the mean angular velocity, $T_{\rm orb}$ one sidereal year, $a$ the Earth's semimajor axis, and $e$ its eccentricity. The right-handed orthonormal vectors $\hat{\boldsymbol{x}},\hat{\boldsymbol{y}}$ are defined so that $\hat{\boldsymbol{x}}$ points from the barycenter to Earth's perihelion, and the true anomaly $\psi(t)$ is measured from that point. The true anomaly does not have a closed-form expression as a function of time for general eccentricity $e > 0$. However, since the Earth's eccentricity is small, $e \sim 10^{-2}$, we can perform a series expansion around the circular case [53],

$$\begin{aligned}\cos\psi &= \cos\omega t + e(\cos 2\omega t - 1) + \mathcal{O}(e^2), \\ \sin\psi &= \sin\omega t + e\sin 2\omega t + \mathcal{O}(e^2), \end{aligned} \quad (12)$$

with the time $t$ chosen such that the Earth is at perihelion at $t = 0$. This gives

$$\begin{aligned}\boldsymbol{v}_{\rm orb} = &-\omega a(\sin\omega t + e\sin 2\omega t)\hat{\boldsymbol{x}} \\ &+ \omega a(\cos\omega t + e\cos 2\omega t)\hat{\boldsymbol{y}} + \mathcal{O}(e^2). \end{aligned} \quad (13)$$

The spherical harmonics of the orbital dipole therefore read

$$\begin{aligned}\Omega_{10}^{(\rm orb)} &= \sqrt{\frac{4\pi}{3}}\frac{\omega a}{v_{\rm sol}}\mathcal{D}_\alpha[-\cos\theta_{\hat{\boldsymbol{x}}}(\sin\omega t + e\sin 2\omega t) \\ &\quad + \cos\theta_{\hat{\boldsymbol{y}}}(\cos\omega t + e\cos 2\omega t)], \\ \Omega_{11}^{(\rm orb)} &= \sqrt{\frac{2\pi}{3}}\frac{\omega a}{v_{\rm sol}}\mathcal{D}_\alpha[+\sin\theta_{\hat{\boldsymbol{x}}}e^{-i\alpha_{\hat{\boldsymbol{x}}}}(\sin\omega t + e\sin 2\omega t) \\ &\quad - \sin\theta_{\hat{\boldsymbol{y}}}e^{-i\alpha_{\hat{\boldsymbol{y}}}}(\cos\omega t + e\cos 2\omega t)], \end{aligned} \quad (14)$$

where $\theta \equiv (\pi/2) - \delta$, and $\alpha_{\hat{\boldsymbol{x}}},\delta_{\hat{\boldsymbol{x}}}$ and $\alpha_{\hat{\boldsymbol{y}}},\delta_{\hat{\boldsymbol{y}}}$ are the equatorial coordinates of the unit vectors $\hat{\boldsymbol{x}},\hat{\boldsymbol{y}}$, which we compute as [53–55]

$$\begin{aligned}\alpha_{\hat{\boldsymbol{x}}} &= 104.06721\ \text{deg}, & \delta_{\hat{\boldsymbol{x}}} &= 22.80924\ \text{deg}, \\ \alpha_{\hat{\boldsymbol{y}}} &= 191.91063\ \text{deg}, & \delta_{\hat{\boldsymbol{y}}} &= -5.11317\ \text{deg}. \end{aligned} \quad (15)$$

For the Earth's orbital parameters, we take [53]

$$\begin{aligned}\omega &= 1.99102 \times 10^{-7}\ \text{Hz}, \\ a &= 1.49598 \times 10^{8}\ \text{km}, \\ e &= 0.01671, \end{aligned} \quad (16)$$

and for the solar dipole velocity, we use the value inferred by *Planck* [36],

$$v_{\rm sol} = 369.82 \pm 0.11\ \text{km s}^{-1} = (1.2336 \pm 0.0004) \times 10^{-3}. \quad (17)$$

Note that the fractional changes in the overall dipole due to the orbital dipole are of the order $\omega a/v_{\rm sol} \approx 8\%$.

In summary, the spherical harmonics associated with the kinematic dipole (solar plus orbital) are

$$\begin{aligned}\Omega_{10}^{(\rm d)} &= -\mathcal{D}_\alpha(0.24745 + 0.06390\sin\omega t + 0.00107\sin 2\omega t + 0.01469\cos\omega t + 0.00025\cos 2\omega t), \\ \Omega_{11}^{(\rm d)} &= \mathcal{D}_\alpha[1.40489 + 0.30011i - (0.02612 + 0.10422i)\sin\omega t - (0.00044 + 0.00174i)\sin 2\omega t \\ &\quad + (0.11359 - 0.02396i)\cos\omega t + (0.00190 - 0.00040i)\cos 2\omega t]. \end{aligned} \quad (18)$$

For a fixed power-law index $\alpha$, there is only one free parameter, the amplitude $\mathcal{D}_\alpha$.

### E. Relationship to the angular power spectrum

The kinematic dipole generates a contribution to the $\ell = 1$ multipole of the GWB angular power spectrum,

$$C_\ell = \frac{1}{2\ell+1}\sum_{m=-\ell}^{+\ell}|\Omega_{\ell m}|^2. \tag{19}$$

Using Eqs. (10) and (14), we calculate the size of this contribution, allowing us to compare the results of our search with the upper limits on $C_1$ obtained by the LVK directional GWB search [46].

For the solar dipole alone, the corresponding angular power is

$$C_1 = \frac{4\pi}{9}\mathcal{D}_\alpha^2. \tag{20}$$

Including the orbital dipole gives rise to time-dependent contributions such that $C_1$ is no longer constant. Many of these time-dependent terms vanish if one integrates over one sidereal year $T_{\rm orb}$, leaving just a small enhancement to the $\ell = 1$ multipole,

$$C_1 \approx \frac{4\pi}{9}\mathcal{D}_\alpha^2\left[1+\left(\frac{\omega a}{v_{\rm sol}}\right)^2\right], \tag{21}$$

where $(\omega a/v_{\rm sol})^2 \approx 6.4\times10^{-3}$ (as above, we have neglected terms of order $e^2$).

## III. SEARCH METHOD

### A. Statistics of cross-correlated strain data

We search for the GWB by cross-correlating data measured by different detectors [7,56], as this allows us to differentiate the GW signal from the noise present in each detector. To do so, we partition each data time series into segments of length $\tau$ (chosen such that $1/\tau$ is much smaller than the GW frequencies we are sensitive to), labeling each segment by its midpoint time $t$. We then analyze these data segments in the Fourier domain, with $f$ labeling the different frequency bins. (We can include only positive frequencies without loss of generality.) For each pair of detectors $(I, J)$, we form the cross-correlation power spectrum estimator,

$$\hat{\mathcal{P}}_{IJ}(f,t) \equiv \frac{2}{\tau}s_I(f,t)s_J^*(f,t), \tag{22}$$

where $s_I(f,t)$ are the Fourier-domain strain data from detector $I$. Assuming zero noise correlation between different detectors [57], the expectation value of $\hat{\mathcal{P}}_{IJ}(f,t)$ reads

$$\begin{aligned}\mathcal{P}_{IJ}(f,t) &\equiv \langle\hat{\mathcal{P}}_{IJ}(f,t)\rangle \\ &= \delta_{IJ}\mathcal{N}_I(f,t) + \mathcal{H}_\alpha(f)\sum_{\ell=0}^{\infty}\sum_{m=-\ell}^{+\ell}\gamma_{\ell m}^{IJ}(f,t)\Omega_{\ell m}(t),\end{aligned} \tag{23}$$

where $\mathcal{N}_I$ is the power spectral density (PSD) of the noise in detector $I$ (which we allow to be nonstationary), and $\Omega_{\ell m}$ are the spherical harmonics of the GWB. The $\gamma_{\ell m}^{IJ}$ are the spherical harmonic components of the *overlap reduction function* (ORF) for detector pair $(I, J)$ [7,56], which describes the average cross-power coherence between the two detectors, as determined by their separation and relative orientations. Note that both sets of spherical harmonics are time dependent; for the ORF, this time dependence is due to the Earth's daily rotation, while for the GWB it is due to the annual modulation of the dipole. The function

$$\mathcal{H}_\alpha(f) \equiv \frac{3H_0^2}{2\pi^2 f_{\rm ref}^3}(f/f_{\rm ref})^{\alpha-3} \tag{24}$$

translates between the signal PSD and GWB energy density spectrum at frequency $f_{\rm ref}$.

Since we are targeting the kinematic dipole, we assume that the spherical harmonics $\Omega_{\ell m}$ in Eq. (23) are given by those we calculated in Sec. II. In what follows, it is convenient to define the signal template,

$$\mathcal{T}_{\alpha,IJ}(f,t) \equiv \frac{\mathcal{H}_\alpha(f)}{\mathcal{D}_\alpha}\sum_{\ell m}\gamma_{\ell m}^{IJ}(f,t)\Omega_{\ell m}^{(\rm d)}(t), \tag{25}$$

which encodes the time and frequency dependence of the response of the detector pair to a dipole with spectral index $\alpha$. This allows us to write Eq. (23) as

$$\mathcal{P}_{IJ} = \delta_{IJ}\mathcal{N}_I + \mathcal{D}_\alpha\mathcal{T}_{\alpha,IJ}, \tag{26}$$

(note that there is no implied sum over $\alpha$).

Assuming the data $s_I(f,t)$ are Gaussian, we calculate the covariance of different correlators (22) using Isserlis' theorem, as

$$\begin{aligned}\mathrm{Cov}[\hat{\mathcal{P}}_{IJ}(f,t),\hat{\mathcal{P}}_{I'J'}(f',t')] &= \delta_{ff'}\delta_{tt'}\mathcal{P}_{II'}(f,t)\mathcal{P}_{JJ'}^*(f,t) \\ &= \delta_{ff'}\delta_{tt'}\delta_{II'}\delta_{JJ'}\mathcal{N}_I\mathcal{N}_J + \mathcal{O}(\mathcal{D}_\alpha).\end{aligned} \tag{27}$$

### B. Maximum-likelihood dipole estimator

The statistics of our complex strain data are defined by a circularly symmetric normal log-likelihood function,

$$\mathcal{L}(s|\mathcal{D}_\alpha) = -\sum_{f,t}\left[\ln(\det(\pi\mathsf{C})) + \sum_{I,J}s_I^*\mathsf{C}_{IJ}^{-1}s_J\right], \tag{28}$$

where the sum is over data segments and positive frequency bins. Here, we have defined the covariance matrix,

$$\mathsf{C}_{IJ} = \langle s_I s_J^* \rangle = \frac{\tau}{2}(\delta_{IJ}\mathcal{N}_I + \mathcal{D}_\alpha \mathcal{T}_{\alpha,IJ}), \tag{29}$$

whose inverse can be written as

$$\mathsf{C}^{-1}_{IJ} = \frac{2}{\tau}\left(\frac{\delta_{IJ}}{\mathcal{N}_I} - \frac{\mathcal{D}_\alpha \mathcal{T}_{\alpha,IJ}}{\mathcal{N}_I \mathcal{N}_J}\right) + \mathcal{O}(\mathcal{D}_\alpha^2). \tag{30}$$

We construct an estimator for the dipole amplitude $\mathcal{D}_\alpha$ by finding the particular value $\hat{\mathcal{D}}_\alpha(s)$ that maximizes this likelihood function for a given realization of the strain data. The simplest way to do this is to find the value for which the derivative $\partial\mathcal{L}/\partial\mathcal{D}_\alpha$ vanishes. Using the standard identities,

$$\frac{\partial}{\partial x}\ln(\det \mathsf{M}) = \mathrm{Tr}\left\{\mathsf{M}^{-1}\frac{\partial \mathsf{M}}{\partial x}\right\},$$
$$\frac{\partial}{\partial x}\mathsf{M}^{-1} = -\mathsf{M}^{-1}\frac{\partial \mathsf{M}}{\partial x}\mathsf{M}^{-1}, \tag{31}$$

we therefore write

$$\frac{\partial\mathcal{L}}{\partial\mathcal{D}_\alpha} = \sum_{f,t}\left[-\sum_{I,J}\mathsf{C}^{-1}_{IJ}\frac{\partial \mathsf{C}_{JI}}{\partial\mathcal{D}_\alpha} + \sum_{I,J,K,L}\mathsf{C}^{-1}_{IJ}\frac{\partial \mathsf{C}_{JK}}{\partial\mathcal{D}_\alpha}\mathsf{C}^{-1}_{KL}\frac{\tau}{2}\hat{\mathcal{P}}_{LI}\right], \tag{32}$$

where we have replaced the strain data $s_I$ with the strain power spectrum estimator $\hat{\mathcal{P}}_{IJ} = (2/\tau)s_I s_J^*$.

Note that Eq. (32) includes the autopower estimators $\hat{\mathcal{P}}_{II}$. In principle, these include a contribution from the dipole signal, as well as from the noise autopower in each detector [cf. Eq. (29)]. In practice, this signal contribution is much smaller than the uncertainty on the noise power, so the autocorrelation terms are not useful in constructing our estimator. We therefore "average them out", replacing them with their mean values and keeping only the cross-correlation terms. Inserting Eqs. (29) and (30) into Eq. (32), we therefore obtain

$$\frac{\partial\mathcal{L}}{\partial\mathcal{D}_\alpha} = \sum_{f,t}\sum_{I\neq J}\frac{\mathcal{T}^*_{\alpha,IJ}(\hat{\mathcal{P}}_{IJ} - \mathcal{D}_\alpha\mathcal{T}_{\alpha,IJ})}{\mathcal{N}_I\mathcal{N}_J} + \mathcal{O}(\mathcal{D}_\alpha^2). \tag{33}$$

This can be written more compactly by defining an inner product,

$$(\mathcal{A}|\mathcal{B}) \equiv \sum_{f,t}\sum_{I\neq J}\frac{\mathcal{A}^*_{IJ}\mathcal{B}_{IJ}}{\mathcal{N}_I\mathcal{N}_J} = 2\sum_{f,t}\sum_{I>J}\mathrm{Re}\left\{\frac{\mathcal{A}^*_{IJ}\mathcal{B}_{IJ}}{\mathcal{N}_I\mathcal{N}_J}\right\}, \tag{34}$$

which describes the noise-weighted coherence between two stochastic cross-power signal models, $\mathcal{A}_{IJ}(f,t)$ and $\mathcal{B}_{IJ}(f,t)$. (The second equality here comes from the fact that exchanging the two detector indices $I, J$ is equivalent to taking a complex conjugate.) We write the associated norm as

$$\|\mathcal{A}\|^2 \equiv (\mathcal{A}|\mathcal{A}). \tag{35}$$

Equation (33) then becomes

$$\frac{\partial\mathcal{L}}{\partial\mathcal{D}_\alpha} = (\mathcal{T}_\alpha|\hat{\mathcal{P}} - \mathcal{D}_\alpha\mathcal{T}_\alpha) + \mathcal{O}(\mathcal{D}_\alpha^2). \tag{36}$$

Setting this to zero, and keeping only the leading-order term in $\mathcal{D}_\alpha$, we therefore obtain our maximum-likelihood estimator for the dipole amplitude,

$$\hat{\mathcal{D}}_\alpha(s) \equiv \frac{(\mathcal{T}_\alpha|\hat{\mathcal{P}}(s))}{\|\mathcal{T}_\alpha\|^2}, \tag{37}$$

where we have emphasised the data dependence of the power spectrum estimator $\hat{\mathcal{P}}_{IJ} \equiv (2/\tau)s_I s_J^*$ on the right-hand side of the above equation.

### C. Sampling distribution of the estimator

A simple calculation shows that our dipole estimator is unbiased,

$$\langle\hat{\mathcal{D}}_\alpha\rangle = \frac{\langle(\mathcal{T}_\alpha|\hat{\mathcal{P}})\rangle}{\|\mathcal{T}_\alpha\|^2} = \frac{(\mathcal{T}_\alpha|\mathcal{D}_\alpha\mathcal{T}_\alpha)}{\|\mathcal{T}_\alpha\|^2} = \mathcal{D}_\alpha. \tag{38}$$

To calculate the variance of the estimator, note that

$$\begin{aligned}\mathrm{Var}[(\mathcal{T}_\alpha|\hat{\mathcal{P}})] &= \sum_{f,f',t,t'}\sum_{I\neq J,I'\neq J'}\frac{\mathcal{T}^*_{\alpha,IJ}\mathcal{T}_{\alpha,I'J'}\mathrm{Cov}[\hat{\mathcal{P}}_{IJ},\hat{\mathcal{P}}_{I'J'}]}{\mathcal{N}_I\mathcal{N}_J\mathcal{N}_{I'}\mathcal{N}_{J'}}\\ &= \sum_{f,t}\sum_{I\neq J}\frac{|\mathcal{T}_{\alpha,IJ}|^2}{\mathcal{N}_I\mathcal{N}_J}(1+\mathcal{O}(\mathcal{D}_\alpha))\\ &= \|\mathcal{T}_\alpha\|^2(1+\mathcal{O}(\mathcal{D}_\alpha)),\end{aligned} \tag{39}$$

where we have used Eq. (27) in the second equality. We therefore have

$$\mathrm{Var}[\hat{\mathcal{D}}_\alpha] = \frac{\mathrm{Var}[(\mathcal{T}_\alpha|\hat{\mathcal{P}})]}{\|\mathcal{T}_\alpha\|^4} = \frac{1}{\|\mathcal{T}_\alpha\|^2}(1+\mathcal{O}(\mathcal{D}_\alpha)). \tag{40}$$

[In what follows, we no longer keep track of $\mathcal{O}(\mathcal{D}_\alpha)$ corrections, as the leading-order term here is sufficient for our analysis.]

Note that, in the weak-signal limit, Eq. (40) saturates the Cramér-Rao bound, which is given here by

$$\mathrm{Var}[\hat{\mathcal{D}}_\alpha] \geq \frac{1}{\langle(\partial\mathcal{L}/\partial\mathcal{D}_\alpha)^2\rangle} = \frac{1}{\mathrm{Var}[(\mathcal{T}_\alpha|\hat{\mathcal{P}})]} = \frac{1}{\|\mathcal{T}_\alpha\|^2}. \tag{41}$$

This shows that $\hat{\mathcal{D}}_\alpha$ is the minimum-variance unbiased estimator for $\mathcal{D}_\alpha$ (as expected for a maximum-likelihood estimator).

We have assumed that the strain data $s$ are Gaussian random variables, which means that the strain power spectrum estimators $\hat{\mathcal{P}}$ are definitively *non*-Gaussian (rather, they follow a $\chi^2$ distribution). However, our dipole estimator is a sum over

$$N \equiv \sum_{f,t} \sum_{I \neq J} \tag{42}$$

independent real degrees of freedom. For large $N$, this means that $\hat{\mathcal{D}}_\alpha$ is asymptotically Gaussian by the central limit theorem. For the LIGO/Virgo O3 dataset, we have $N \sim 10^{10}$, so the Gaussian approximation is extremely accurate.[5] This means that the mean and variance fully specify the sampling distribution of $\hat{\mathcal{D}}_\alpha$.

### D. Signal-to-noise ratio and upper limits

It is convenient to define the signal-to-noise ratio (SNR) of our search,[6]

$$\rho_\alpha \equiv \frac{\hat{\mathcal{D}}_\alpha}{\sqrt{\mathrm{Var}[\hat{\mathcal{D}}_\alpha]}} = \frac{(\mathcal{T}_\alpha|\hat{\mathcal{P}})}{\|\mathcal{T}_\alpha\|}. \tag{43}$$

Given the results above, we see that in the absence of a signal ($\mathcal{D}_\alpha = 0$) this follows a standard normal distribution, $\rho_\alpha \sim \mathrm{N}(0,1)$, which is very convenient for interpreting the statistical significance of a given search result. If a signal is present, then the expected SNR, $\langle \rho_\alpha \rangle = \mathcal{D}_\alpha \|T_\alpha\|$, scales as the square root of the total observation time, due to the increasing number of terms that are summed over in the inner product. We therefore recover the standard SNR $\propto \sqrt{T_{\mathrm{obs}}}$ scaling from other stochastic searches.

If we observe a SNR, $\rho_{\alpha,\mathrm{obs}}$, that is not high enough to claim a detection, then we can instead set an upper limit by noting that, for a given value of $\mathcal{D}_\alpha$,

$$\Pr(\rho_\alpha \geq \rho_{\alpha,\mathrm{obs}}|\mathcal{D}_\alpha) = \frac{1}{2}\left[1 + \mathrm{erf}\left(\frac{\mathcal{D}_\alpha\|\mathcal{T}_\alpha\| - \rho_{\alpha,\mathrm{obs}}}{\sqrt{2}}\right)\right]. \tag{44}$$

For a given confidence level $p \in (0,1)$, the corresponding upper limit on $\mathcal{D}_\alpha$ is obtained by setting (44) equal to $p$ and then solving for $\mathcal{D}_\alpha$, e.g., for $p = 0.95$,

$$\mathcal{D}_\alpha^{95\mathrm{UL}} \equiv \frac{\rho_{\alpha,\mathrm{obs}} + \sqrt{2}\mathrm{erf}^{-1}(2 \times 0.95 - 1)}{\|\mathcal{T}_\alpha\|}. \tag{45}$$

### E. Geometric interpretation

The inner product that we have introduced in Eq. (34) defines an $N$-dimensional vector space, in which individual vectors represent different possible cross-power signal models for our detector network. In light of this, our search SNR (43) has the simple geometric interpretation of projecting the cross-correlated data onto the "$\mathcal{T}_\alpha$ direction" in this space; i.e., the direction corresponding to our kinematic dipole signal template.

Using Eqs. (23) and (27) we see that, in the absence of a signal, the cross-correlated data vector $\hat{\mathcal{P}}$ has a mean square length of

$$\langle \|\hat{\mathcal{P}}\|^2 \rangle = N, \tag{46}$$

as one would expect for a random walk of $N$ steps of unit length. This is because each term which is summed over in the inner product has unit mean,

$$\frac{\langle |\hat{\mathcal{P}}_{IJ}|^2 \rangle}{\mathcal{N}_I \mathcal{N}_J} = 1, \tag{47}$$

i.e., for each of the $N$ dimensions of the signal space, the data vector takes a statistically independent random step with zero mean and unit variance. The detection statistic measures the projection of this random walk onto one of these $N$ directions (that parallel to the template vector $\mathcal{T}_\alpha$), which explains why $\rho_\alpha \sim \mathrm{N}(0,1)$ in the absence of a signal. If a signal is present, then it causes the random walk to travel preferentially in the $\mathcal{T}_\alpha$ direction and gives a positive offset in the corresponding inner product.

### F. Bias from ignoring the orbital dipole

One advantage of the method described above over existing searches is that it allows for a time-dependent signal model, enabling us to capture the annual modulation of the dipole signal due to the Earth's orbital motion. We can calculate the bias which would be introduced if one ignored this orbital contribution by writing

$$\text{relative error} = \frac{\hat{\mathcal{D}}_\alpha^{(\mathrm{sol})} - \mathcal{D}_\alpha}{\mathcal{D}_\alpha} = \frac{(\mathcal{T}_\alpha^{(\mathrm{sol})}|\hat{\mathcal{P}})}{\mathcal{D}_\alpha\|\mathcal{T}_\alpha^{(\mathrm{sol})}\|^2} - 1, \tag{48}$$

where $\mathcal{D}_\alpha$ is the true value of the dipole amplitude, and $\hat{\mathcal{D}}_\alpha^{(\mathrm{sol})}$ is the value inferred using a template, $\mathcal{T}_\alpha^{(\mathrm{sol})}$, which only includes the solar dipole. Since $\langle \hat{\mathcal{P}} \rangle = \mathcal{D}_\alpha \mathcal{T}_\alpha$, we find that

[5]This assumes ~1 yr of observation with three detectors, using $\tau = 192$ s intervals, with frequency resolution $1/32$ Hz in the band 20–1726 Hz [41].

[6]This is completely analogous to the standard matched-filter SNR one usually defines for coherent GW signals—the difference here being that the inner product captures *strain power coherence* over a detector network, rather than *strain coherence* in a single detector.

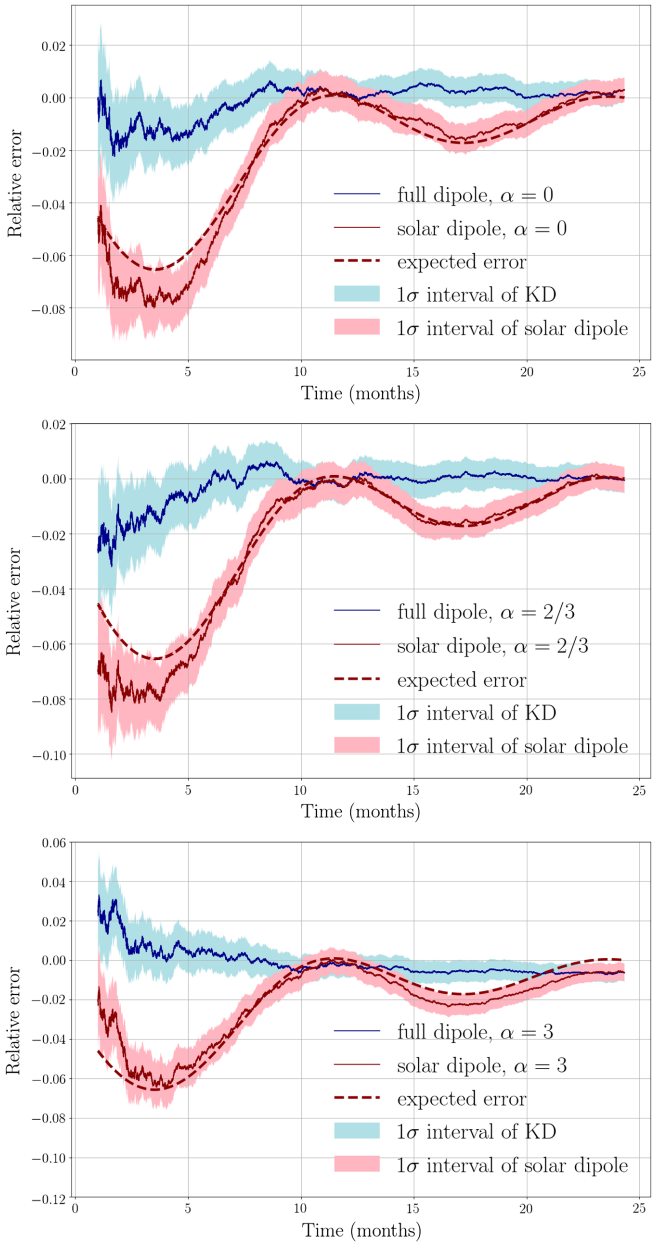


FIG. 2. Relative error of our targeted kinematic dipole search as a function of observing time for simulated data containing a kinematic dipole signal $\mathcal{D}_\alpha = 3.1 \times 10^{-8}$ for $\alpha = 0$ (top panel), $\mathcal{D}_\alpha = 2.3 \times 10^{-8}$ for $\alpha = 2/3$ (middle panel), and $\mathcal{D}_\alpha = 4 \times 10^{-9}$ for $\alpha = 3$ (bottom panel). The blue and red traces correspond to analyses using the full (time-dependent) dipole template and the (time-independent) solar dipole template, respectively. While the relative errors for the full dipole template analyses converge to zero rapidly, those obtained using the solar-dipole template show a relative error consistent with the expected error (48) (dashed red line).

$$\langle \text{relative error} \rangle = \frac{(\mathcal{T}_\alpha^{(\text{sol})} | \mathcal{T}_\alpha)}{\|\mathcal{T}_\alpha^{(\text{sol})}\|^2} - 1. \tag{49}$$

In Sec. IV B, and Fig. 2, we further investigate this relative error using simulated data.

## IV. APPLICATION TO REAL AND SIMULATED DATA

### A. Data processing

When applying our data analysis pipeline to either real or (semirealistic) simulated data, several standard data-processing procedures need to be performed. First, we divide the time-domain data into shorter segments, typically of duration 192 seconds. To suppress spectral leakage, we Hann window the data, overlapping the windowed segments by 50% to avoid losing roughly half of the data due to the effects of the tapering. The windowed data are then transformed into the frequency-domain data via the short-time Fourier transform and coarse-grained to a frequency resolution of $1/32$ Hz as described in [41–46]. Since the data have been windowed, the cross-correlation power estimate (37) and its variance (40) need to be multiplied by windowing factors [58]. Second, to avoid a bias when computing the variance, we multiply $\sigma_{\mathcal{D}_\alpha}$ by a bias factor of 1.0504 [59]. The detection statistic and variance of the overlapped data segments are then optimally combined as described in [60].

### B. Simulated data

We first validate our analysis method and the corresponding data analysis pipeline by performing a targeted dipole search on mock data which contain a GWB with a known kinematic dipole. For the purpose of this exercise, we simulate a dipole with $\mathcal{D}_\alpha = 3.1 \times 10^{-8}$, $2.3 \times 10^{-8}$, and $4 \times 10^{-9}$, respectively, for $\alpha = 0$, $2/3$, and 3. These values of $\mathcal{D}_\alpha$ are chosen so that each dipole has approximately the same accumulated SNR. The mock data cover two years, with a start time equal to the start of LIGO/Virgo's third observing run (O3). To ensure the gravitational-wave intensity is positive for all sky directions, we include a monopole moment with value $2\sqrt{4\pi}\mathcal{D}_\alpha$. We estimate the dipole moment for each spectral index using both the full time-dependent dipole template (18) and the time-independent solar dipole template (10).

Figure 2 shows the relative error of the point estimate, $(\hat{\mathcal{D}}_\alpha - \mathcal{D}_\alpha)/\mathcal{D}_\alpha$, as a function of observation time, as obtained using the full dipole template (solid blue line) and the solar dipole template (solid red line). The shaded regions show the $1\sigma$ uncertainty in each case, $1/\|\mathcal{T}_\alpha\|$.

From Fig. 2, we can draw the following two conclusions: First, the relative error using the full dipole template converges to zero very rapidly. This suggests that our data analysis pipeline can accurately and swiftly recover the injected value of $\mathcal{D}_\alpha$ for all three spectral indices. Second, the expected errors predicted using Eq. (48) (dashed red lines) are consistent with the measured errors within $\sim 1\sigma$, which suggests that the measured relative errors are as expected. Thus, our analysis method can accurately and efficiently measure the dipole moment using the full time-dependent template, avoiding the bias that would result if

TABLE I. Results of searching for the kinetic dipole using data from the first three observing runs of the Advanced LIGO and Virgo detectors. Columns from left to right are (i) spectral indices of the GW background energy-density spectrum, (ii) observed values of the detection statistic $\rho_{\alpha,\mathrm{obs}}$, (iii) point estimates of the kinematic dipole moment $\hat{\mathcal{D}}_\alpha$, (iv) measurement uncertainties of the kinematic dipole moment $\sigma_{\mathcal{D}_\alpha}$, (v) 95% confidence-level upper limits on the dipole angular power spectrum component $C_1$, converted from the measurement of $\mathcal{D}_\alpha$ as described in the main text, and (vi) 95% confidence-level upper limits on $C_1$, as determined using the spherical-harmonic decomposition (SHD) approach [46,61].

| $\alpha$ | $\rho_{\alpha,\mathrm{obs}}$ | $\hat{\mathcal{D}}_\alpha$ | $\sigma_{\mathcal{D}_\alpha}$ | $C_1^{95\mathrm{UL}}$ | $C_1^{95\mathrm{UL}}$ (SHD) |
|---|---|---|---|---|---|
| 0 | 0.0579 | $6.58 \times 10^{-11}$ | $1.14 \times 10^{-9}$ | $5.23 \times 10^{-18}$ | $1.88 \times 10^{-18}$ |
| 2/3 | 0.442 | $3.32 \times 10^{-10}$ | $7.51 \times 10^{-10}$ | $3.43 \times 10^{-18}$ | $1.38 \times 10^{-18}$ |
| 3 | 0.426 | $4.09 \times 10^{-11}$ | $9.58 \times 10^{-11}$ | $5.50 \times 10^{-20}$ | $7.22 \times 10^{-20}$ |

we ignore the orbital dipole, which can be as large as $\mathcal{O}(10\%)$.

### C. LIGO/Virgo data

Having validated our data analysis method and pipeline, we apply the formalism described in the previous sections to search for evidence of the kinematic dipole using data taken by the Advanced LIGO and Virgo detectors during their first three observing runs (O1, O2, and O3) [41–46]. To avoid data contamination due to narrow-band noise sources (harmonics of the 60 and 50 Hz power mains, resonances due to mirror suspensions, calibration lines, etc.), the frequencies corresponding to instrumental lines [61,62] are notched. Data segments which contain non-Gaussian noise artifacts (such as glitches) or resolvable signals from individual GW events are also excluded from the analysis (see also [63–66]). For simplicity, we neglect the impact of calibration uncertainty in the LIGO/Virgo interferometers in this analysis. However, for future applications of our pipeline, it is straightforward to perform a Bayesian marginalization over this uncertainty using existing tools [41,46]. This marginalization typically increases the final uncertainty (and associated upper limits) by at most a few percent.

Table I summarizes the results of our search. The columns show the three spectral indices $\alpha$ of the GW energy-density spectrum searched for, the observed signal-to-noise ratio $\rho_{\alpha,\mathrm{obs}}$, the corresponding point estimates for the dipole amplitude $\hat{\mathcal{D}}_\alpha$ and their uncertainties $\sigma_{\mathcal{D}_\alpha}$, and the 95% confidence upper limits (ULs) for $C_1$ calculated for our kinematic dipole search and (for comparison) the standard LIGO/Virgo spherical harmonic search. Since $|\rho_{\alpha,\mathrm{obs}}|$ is significantly less than unity, we conclude that we have not detected a kinematic dipole signal, which is consistent with the nondetection of a GWB reported in [41,46]. Our results for $\mathcal{D}_\alpha$ can be converted to an UL on the dipole-angular power spectrum component $C_1$ by simply using Eq. (20),

$$C_1^{95\mathrm{UL}} = \frac{4\pi}{9}(\mathcal{D}_\alpha^{95\mathrm{UL}})^2. \tag{50}$$

[This is consistent with using Eq. (21) to less than 1%.] These 95% confidence ULs can be compared to similar ULs calculated using the spherical harmonic decomposition (SHD) method (right-most column) [46].[7] We see that our results are consistent with the existing measurement of anisotropies in the GWB.

### D. Forecasts for third-generation interferometers

Given the null results reported above, it is interesting to ask how much we can expect our sensitivity to improve with next-generation gravitational-wave observatories such as the Einstein Telescope [67] and Cosmic Explorer [68]. (For the Einstein Telescope, we assume an L-shaped geometry and use the sensitivity curve available at [69].) It is straightforward to forecast the expected upper limits obtained by a given interferometer network using Eq. (45). In Fig. 3, we compute these forecasts as a function of observing time for a third-generation network consisting of one Einstein Telescope and two Cosmic Explorers. For the purposes of computing the overlap reduction functions, we assume that the Einstein Telescope is located at the current Virgo site, while the two Cosmic Explorers are located at the current sites of the two LIGO interferometers; however, we do not expect our results to be overly sensitive to this choice. We find that this network will be sensitive to $\mathcal{D} \approx 3 \times 10^{-14}$ after one year of observations, with some slight variation between different spectral indices—an improvement of three orders of magnitude over our current constraints from LIGO/Virgo.

In Fig. 3, we also show the predicted dipole from inspiraling compact binaries (7), whose amplitude we take

[7]The values of $C_1^{95\mathrm{UL}}$ (SHD) listed in the last column are not the square of $C_1^{1/2}$ from Fig. 4 of [46], which take into account detector calibration error. Since we do not include the effect of calibration error in our measurement, we also do not include it for the SHD analysis. Instead, we use

$$\begin{aligned} C_1^{95\mathrm{UL}}(\mathrm{SHD}) &= \hat{C}_1 + \sqrt{2}\mathrm{erf}^{-1}(2 \times 0.95 - 1)\sigma_{C_1} \\ &= \hat{C}_1 + 1.64\sigma_{C_1}, \end{aligned}$$

where $\hat{C}_1$ and $\sigma_{C_1}$ are taken from [61].

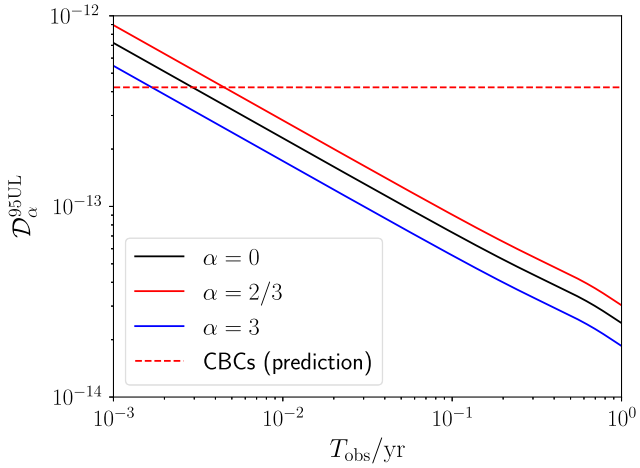


FIG. 3. Forecast upper limits (95% confidence) on the dipole amplitude with a third-generation interferometer network (Einstein Telescope + two Cosmic Explorers). The predicted dipole from compact binary coalescences is, in principle, accessible with less than two days of data.

as $\mathcal{D}_{2/3} \approx 4 \times 10^{-13}$ [34]. (This value is based on our current understanding of the likely amplitude of the monopole component and is therefore subject to some modeling uncertainty but should be robust to within an order of magnitude.) We see that our third-generation network is expected to detect this dipole extremely quickly, with less than two days of data. This shows that future gravitational-wave observatories will be capable of measuring this particular dipole with very high precision, enabling robust tests of our understanding of the source population and of cosmology more broadly (i.e., by testing whether the dipole direction and amplitude are consistent with that of the CMB or whether they exhibit anomalies similar to those discussed in [37–39]).[8]

## V. CONCLUSION

In this paper, we have constructed a targeted search pipeline for the kinematic dipole of the gravitational-wave background induced by the motion of the Earth relative to the cosmic rest frame, accounting for both the motion of the solar system barycenter and the Earth's orbit with respect to this. The former is the main contribution to the induced dipole, while the latter gives rise to an annual modulation, which we incorporate by generalizing the existing search formalism. By applying our pipeline to mock data, we have shown that we can accurately and efficiently measure the simulated dipole moment, whereas the existing methods, by neglecting the orbital dipole of the dipole signal, result in a bias as large as $\mathcal{O}(10\%)$. A further advantage of our method over existing searches is that, by constructing an explicit signal template on the sky, we avoid various regularization issues associated with generic spherical harmonic searches due to effective "blind spots" in the response of the detector network. Instead, our search returns a single, unambiguous measurement of the dipole amplitude. Our analysis can also be straightforwardly adapted to perform a targeted search for any time- and frequency-dependent stochastic signal with a known sky pattern, e.g., GW emission from the Galactic Center [70,71]. It is also straightforward to replace the *Planck* values we have assumed for the dipole magnitude and direction with any other desired values, which may be relevant given the claimed tension between *Planck* and various lower-redshift surveys [37–39].

We have applied our pipeline to data from LIGO/Virgo's first three observing runs and find no evidence for a dipole signal. However, looking forward to upcoming third-generation interferometers, we have shown that our search will be sensitive to dipoles as small as $\mathcal{D}_\alpha \sim 10^{-14}$, providing a novel probe of cosmology and gravitational-wave source physics. In particular, for GWB signals with unknown source physics, a joint measurement of the monopole and the dipole will allow us to extract information about the emission spectra of the sources, whereas for GWB signals that are well understood (e.g., the signal from inspiralling compact binaries), we can instead attempt to provide an independent measurement of our peculiar motion with respect to the cosmic rest frame, allowing us to weigh in on the "dipole tension" discussed above.

We have not considered here the impact of shot noise, which will be important for the kinematic dipole from compact binaries [31]. However, in the context of third-generation interferometers, it is expected that many of the binaries which make up this "stochastic" signal will in fact be individually resolvable, allowing us to coherently subtract them and search for underlying cosmological signals [72,73], to which our dipole search can be applied. Alternatively, it may be possible to mitigate the effects of shot noise by optimally combining data from different time segments [32] and frequency bins [35]. We leave a fuller exploration of these issues for future work.

## ACKNOWLEDGMENTS

A. K.-W. C. thanks Andrew Matas, Erik Floden, and Patrick Meyers for help in analyzing mock and actual data of the Advanced LIGO and Advanced Virgo detectors and Stuart Anderson for coordinating the file I/O on the CIT clusters. The authors acknowledge use of data, software, and web tools from the GW Open Science Center (https://www.gw-openscience.org), a service of LIGO Laboratory, the LIGO Scientific Collaboration, and the Virgo Collaboration. The authors are grateful for computational resources provided by the LIGO Laboratory and supported

[8]Note that we have not investigated here the impact of shot noise on the kinematic dipole from compact binaries [31,32]; we leave this for future work.

by National Science Foundation Grants No. PHY-0757058 and No. PHY-0823459.

A. K.-W. C. is supported by the Hong Kong Scholarship for Excellence Scheme (HKSES). J. D. R. is supported in part by start-up funds provided by Texas Tech University and National Science Foundation Grant No. PHY-2207270. M. S. is supported in part by the Science and Technology Facility Council (STFC), United Kingdom, under the research Grant No. ST/P000258/1. This work was partly enabled by the UCL Cosmoparticle Initiative.

This paper has a LIGO document number LIGO-P2200215 and a KCL document number KCL-PH-TH/2022-38. This material is based upon work supported by NSF's LIGO Laboratory which is a major facility fully funded by the National Science Foundation. This paper has an Einstein Telescope number ET-0169A-22.

[1] B. P. Abbott *et al.* (LIGO, Virgo Collaborations), GWTC-1: A Gravitational-Wave Transient Catalog of Compact Binary Mergers Observed by LIGO and Virgo during the First and Second Observing Runs, Phys. Rev. X **9**, 031040 (2019).

[2] R. Abbott *et al.* (LIGO, Virgo Collaborations), GWTC-2: Compact Binary Coalescences Observed by LIGO and Virgo During the First Half of the Third Observing Run, Phys. Rev. X **11**, 021053 (2021).

[3] R. Abbott *et al.* (LIGO, Virgo Collaborations), GWTC-2.1: Deep extended catalog of compact binary coalescences observed by LIGO and Virgo during the first half of the third observing run, arXiv:2108.01045.

[4] R. Abbott *et al.* (LIGO Scientific, Virgo, KAGRA Collaborations), GWTC-3: Compact binary coalescences observed by LIGO and Virgo during the second part of the third observing run, arXiv:2111.03606.

[5] B. Allen, The Stochastic gravity wave background: Sources and detection, in Les Houches School of Physics: Astrophysical Sources of Gravitational Radiation (1996), pp. 373–417, arXiv:gr-qc/9604033.

[6] M. Maggiore, Gravitational wave experiments and early universe cosmology, Phys. Rep. **331**, 283 (2000).

[7] J. D. Romano and N. J. Cornish, Detection methods for stochastic gravitational-wave backgrounds: A unified treatment, Living Rev. Relativity **20**, 2 (2017).

[8] N. Christensen, Stochastic gravitational wave backgrounds, Rep. Prog. Phys. **82**, 016903 (2019).

[9] A. I. Renzini, B. Goncharov, A. C. Jenkins, and P. M. Meyers, Stochastic gravitational-wave backgrounds: Current detection efforts and future prospects, Galaxies **10**, 34 (2022).

[10] T. Regimbau, The astrophysical gravitational wave stochastic background, Res. Astron. Astrophys. **11**, 369 (2011).

[11] K. Martinovic, C. Perigois, T. Regimbau, and M. Sakellariadou, Footprints of population III stars in the gravitational-wave background, arXiv:2109.09779.

[12] C. Caprini and D. G. Figueroa, Cosmological backgrounds of gravitational waves, Classical Quantum Gravity **35**, 163001 (2018).

[13] R. Abbott *et al.* (LIGO, Virgo, KAGRA Collaborations), Constraints on Cosmic Strings Using Data from the Third Advanced LIGO–Virgo Observing Run, Phys. Rev. Lett. **126**, 241102 (2021).

[14] A. Romero, K. Martinovic, T. A. Callister, H.-K. Guo, M. Martínez, M. Sakellariadou, F.-W. Yang, and Y. Zhao, Implications for First-Order Cosmological Phase Transitions from the Third LIGO-Virgo Observing Run, Phys. Rev. Lett. **126**, 151301 (2021).

[15] K. Martinovic, C. Badger, M. Sakellariadou, and V. Mandic, Searching for parity violation with the LIGO-Virgo-KAGRA network, Phys. Rev. D **104**, L081101 (2021).

[16] A. Romero-Rodriguez, M. Martinez, O. Pujolàs, M. Sakellariadou, and V. Vaskonen, Search for a Scalar Induced Stochastic Gravitational Wave Background in the Third LIGO-Virgo Observing Run, Phys. Rev. Lett. **128**, 051301 (2022).

[17] M. Sakellariadou, Gravitational waves: The theorist's Swiss knife, Universe **8**, 132 (2022).

[18] G. Cusin, C. Pitrou, and J.-P. Uzan, Anisotropy of the astrophysical gravitational wave background: Analytic expression of the angular power spectrum and correlation with cosmological observations, Phys. Rev. D **96**, 103019 (2017).

[19] G. Cusin, C. Pitrou, and J.-P. Uzan, The signal of the gravitational wave background and the angular correlation of its energy density, Phys. Rev. D **97**, 123527 (2018).

[20] A. C. Jenkins and M. Sakellariadou, Anisotropies in the stochastic gravitational-wave background: Formalism and the cosmic string case, Phys. Rev. D **98**, 063509 (2018).

[21] G. Cusin, I. Dvorkin, C. Pitrou, and J.-P. Uzan, First Predictions of the Angular Power Spectrum of the Astrophysical Gravitational Wave Background, Phys. Rev. Lett. **120**, 231101 (2018).

[22] M. Geller, A. Hook, R. Sundrum, and Y. Tsai, Primordial Anisotropies in the Gravitational Wave Background from Cosmological Phase Transitions, Phys. Rev. Lett. **121**, 201303 (2018).

[23] A. C. Jenkins, M. Sakellariadou, T. Regimbau, and E. Slezak, Anisotropies in the astrophysical gravitational-wave background: Predictions for the detection of compact binaries by LIGO and Virgo, Phys. Rev. D **98**, 063501 (2018).

[24] A. C. Jenkins, R. O'Shaughnessy, M. Sakellariadou, and D. Wysocki, Anisotropies in the Astrophysical Gravitational-Wave Background: The Impact of Black Hole Distributions, Phys. Rev. Lett. **122**, 111101 (2019).

[25] N. Bartolo, D. Bertacca, V. De Luca, G. Franciolini, S. Matarrese, M. Peloso, A. Ricciardone, A. Riotto, and G. Tasinato, Gravitational wave anisotropies from primordial black holes, J. Cosmol. Astropart. Phys. 02 (2020) 028.

[26] D. Bertacca, A. Ricciardone, N. Bellomo, A. C. Jenkins, S. Matarrese, A. Raccanelli, T. Regimbau, and M. Sakellariadou, Projection effects on the observed angular spectrum of the astrophysical stochastic gravitational wave background, Phys. Rev. D **101**, 103513 (2020).
[27] N. Bartolo, D. Bertacca, S. Matarrese, M. Peloso, A. Ricciardone, A. Riotto, and G. Tasinato, Anisotropies and non-Gaussianity of the cosmological gravitational wave background, Phys. Rev. D **100**, 121501 (2019).
[28] N. Bartolo, D. Bertacca, S. Matarrese, M. Peloso, A. Ricciardone, A. Riotto, and G. Tasinato, Characterizing the cosmological gravitational wave background: Anisotropies and non-Gaussianity, Phys. Rev. D **102**, 023527 (2020).
[29] N. Bellomo, D. Bertacca, A. C. Jenkins, S. Matarrese, A. Raccanelli, T. Regimbau, A. Ricciardone, and M. Sakellariadou, CLASS_GWB: Robust modeling of the astrophysical gravitational wave background anisotropies, J. Cosmol. Astropart. Phys. 06 (2022) 030.
[30] N. Bartolo *et al.* (LISA Cosmology Working Group Collaboration), Probing anisotropies of the stochastic gravitational wave background with LISA, arXiv:2201.08782.
[31] A. C. Jenkins and M. Sakellariadou, Shot noise in the astrophysical gravitational-wave background, Phys. Rev. D **100**, 063508 (2019).
[32] A. C. Jenkins, J. D. Romano, and M. Sakellariadou, Estimating the angular power spectrum of the gravitational-wave background in the presence of shot noise, Phys. Rev. D **100**, 083501 (2019).
[33] G. Cusin and G. Tasinato, Doppler boosting the stochastic gravitational wave background, J. Cosmol. Astropart. Phys. 08 (2022) 036.
[34] A. C. Jenkins, Cosmology and fundamental physics in the era of gravitational-wave astronomy, Ph.D. thesis, King's Coll. London (2022), https://kclpure.kcl.ac.uk/portal/en/theses/cosmology-and-fundamental-physics-in-the-era-of-gravitationalwave-astronomy(39b9da34-05c4-4887-afe8-7bdcf4cad4c4).html.
[35] L. Valbusa Dall'Armi, A. Ricciardone, and D. Bertacca, The dipole of the astrophysical gravitational-wave background, arXiv:2206.02747.
[36] N. Aghanim *et al.* (Planck Collaboration), Planck 2018 results. I. Overview and the cosmological legacy of Planck, Astron. Astrophys. **641**, A1 (2020).
[37] N. J. Secrest, S. von Hausegger, M. Rameez, R. Mohayaee, S. Sarkar, and J. Colin, A test of the cosmological principle with quasars, Astrophys. J. Lett. **908**, L51 (2021).
[38] C. Dalang and C. Bonvin, On the kinematic cosmic dipole tension, Mon. Not. R. Astron. Soc. **512**, 3895 (2022).
[39] N. Secrest, S. von Hausegger, M. Rameez, R. Mohayaee, and S. Sarkar, A challenge to the standard cosmological model, arXiv:2206.05624.
[40] J. Darling, The universe is brighter in the direction of our motion: Galaxy counts and fluxes are consistent with the CMB dipole, Astrophys. J. Lett. **931**, L14 (2022).
[41] R. Abbott *et al.* (LIGO, Virgo, KAGRA Collaborations), Upper limits on the isotropic gravitational-wave background from Advanced LIGO and Advanced Virgo's third observing run, Phys. Rev. D **104**, 022004 (2021).
[42] B. P. Abbott *et al.* (LIGO, Virgo Collaborations), Upper Limits on the Stochastic Gravitational-Wave Background from Advanced LIGO's First Observing Run, Phys. Rev. Lett. **118**, 121101 (2017); **119**, 029901(E) (2017).
[43] B. P. Abbott *et al.* (LIGO, Virgo Collaborations), Search for the isotropic stochastic background using data from Advanced LIGO's second observing run, Phys. Rev. D **100**, 061101 (2019).
[44] B. P. Abbott *et al.* (LIGO, Virgo Collaborations), Directional Limits on Persistent Gravitational Waves from Advanced LIGO's First Observing Run, Phys. Rev. Lett. **118**, 121102 (2017).
[45] B. P. Abbott *et al.* (LIGO, Virgo Collaborations), Directional limits on persistent gravitational waves using data from Advanced LIGO's first two observing runs, Phys. Rev. D **100**, 062001 (2019).
[46] R. Abbott *et al.* (LIGO, Virgo, KAGRA Collaborations), Search for anisotropic gravitational-wave backgrounds using data from Advanced LIGO and Advanced Virgo's first three observing runs, Phys. Rev. D **104**, 022005 (2021).
[47] P. A. R. Ade *et al.* (Planck Collaboration), Planck 2015 results. XIII. Cosmological parameters, Astron. Astrophys. **594**, A13 (2016).
[48] E. S. Phinney, A practical theorem on gravitational wave backgrounds, arXiv:astro-ph/0108028.
[49] A. Buonanno, G. Sigl, G. G. Raffelt, H.-T. Janka, and E. Muller, Stochastic gravitational wave background from cosmological supernovae, Phys. Rev. D **72**, 084001 (2005).
[50] T. Callister, L. Sammut, S. Qiu, I. Mandel, and E. Thrane, The Limits of Astrophysics with Gravitational-Wave Backgrounds, Phys. Rev. X **6**, 031018 (2016).
[51] V. Cardoso and A. Maselli, Constraints on the astrophysical environment of binaries with gravitational-wave observations, Astron. Astrophys. **644**, A147 (2020).
[52] J. Huang, M. C. Johnson, L. Sagunski, M. Sakellariadou, and J. Zhang, Prospects for axion searches with Advanced LIGO through binary mergers, Phys. Rev. D **99**, 063013 (2019).
[53] C. D. Murray and S. F. Dermott, *Solar System Dynamics* (Cambridge University Press, Cambridge, England, 2000).
[54] T. P. Robitaille *et al.* (Astropy Collaboration), Astropy: A community Python package for astronomy, Astron. Astrophys. **558**, A33 (2013).
[55] A. M. Price-Whelan *et al.* (Astropy Collaboration), The astropy project: Building an open-science project and status of the v2.0 core package, Astron. J. **156**, 123 (2018).
[56] B. Allen and J. D. Romano, Detecting a stochastic background of gravitational radiation: Signal processing strategies and sensitivities, Phys. Rev. D **59**, 102001 (1999).
[57] P. M. Meyers, K. Martinovic, N. Christensen, and M. Sakellariadou, Detecting a stochastic gravitational-wave background in the presence of correlated magnetic noise, Phys. Rev. D **102**, 102005 (2020).
[58] B. Abbott *et al.* (LIGO Collaboration), Analysis of first LIGO science data for stochastic gravitational waves, Phys. Rev. D **69**, 122004 (2004).
[59] A. Lazzarini (LIGO Collaboration), Bias from power spectrum measurement in parameter estimation for the stochastic gravitational wave background, https://dcc.ligo.org/LIGO-T040128/public (2004).

[60] A. Lazzarini and J. Romano (LIGO), Use of overlapping windows in the stochastic background search, https://dcc.ligo.org/T040089/public (2004).
[61] R. Abbott *et al.* (LIGO, Virgo, KAGRA Collaborations), Data products and supplemental information for O3 stochastic directional paper, https://dcc.ligo.org/LIGO-G2002165/public (2021).
[62] R. Abbott *et al.* (LIGO Collaboration), Data for 'Search for the isotropic stochastic background using data from Advanced LIGO's second observing run', https://dcc.ligo.org/T1900058/public (2019).
[63] B. P. Abbott *et al.* (LIGO, Virgo Collaborations), Characterization of transient noise in Advanced LIGO relevant to gravitational wave signal GW150914, Classical Quantum Gravity **33**, 134001 (2016).
[64] E. Thrane, N. Christensen, and R. Schofield, Correlated magnetic noise in global networks of gravitational-wave interferometers: Observations and implications, Phys. Rev. D **87**, 123009 (2013).
[65] E. Thrane, N. Christensen, R. M. S. Schofield, and A. Effler, Correlated noise in networks of gravitational-wave detectors: subtraction and mitigation, Phys. Rev. D **90**, 023013 (2014).
[66] C. Biwer *et al.* (LIGO Collaboration), Validating gravitational-wave detections: The advanced ligo hardware injection system, https://dcc.ligo.org/LIGO-P1600285/public (2016).
[67] M. Punturo *et al.*, The Einstein Telescope: A third-generation gravitational wave observatory, Classical Quantum Gravity **27**, 194002 (2010).
[68] D. Reitze *et al.*, Cosmic explorer: The U.S. contribution to gravitational-wave astronomy beyond LIGO, Bull. Am. Astron. Soc. **51**, 035 (2019), https://baas.aas.org/pub/2020n7i035.
[69] ET Design Team, ET-D sensitivity curve, https://apps.et-gw.eu/tds/?content=3&r=14065 (2018).
[70] D. Talukder, E. Thrane, S. Bose, and T. Regimbau, Measuring neutron-star ellipticity with measurements of the stochastic gravitational-wave background, Phys. Rev. D **89**, 123008 (2014).
[71] D. Agarwal, J. Suresh, V. Mandic, A. Matas, and T. Regimbau, Targeted search for the stochastic gravitational-wave background from the galactic millisecond pulsar population, Phys. Rev. D **106**, 043019 (2022).
[72] X.-J. Zhu, E. J. Howell, D. G. Blair, and Z.-H. Zhu, On the gravitational wave background from compact binary coalescences in the band of ground-based interferometers, Mon. Not. R. Astron. Soc. **431**, 882 (2013).
[73] T. Regimbau, M. Evans, N. Christensen, E. Katsavounidis, B. Sathyaprakash, and S. Vitale, Digging Deeper: Observing Primordial Gravitational Waves Below the Binary Black Hole Produced Stochastic Background, Phys. Rev. Lett. **118**, 151105 (2017).